Impacts of Atmospheric Rivers on Precipitation in Southern South America

MAXIMILIANO VIALE

Instituto Argentino de Nivología, Glaciología y Ciencias Ambientales, CCT–CONICET, Mendoza, Argentina, and Departamento de Geofísica, Universidad de Chile, Santiago, Chile

RAÚL VALENZUELA AND RENÉ D. GARREAUD

Departamento de Geofísica, and Centro del Clima y la Resiliencia, Universidad de Chile, Santiago, Chile

F. MARTIN RALPH

Center for Western Weather and Water Extremes, Scripps Institution of Oceanography, University of California, San Diego, La Jolla, California

(Manuscript received 16 January 2018, in final form 5 September 2018)

ABSTRACT

This study quantifies the impact of atmospheric rivers (ARs) on precipitation in southern South America. An AR detection algorithm was developed based on integrated water vapor transport (IVT) from 6-hourly CFSR reanalysis data over a 16-yr period (2001–16). AR landfalls were linked to precipitation using a comprehensive observing network that spanned large variations in terrain along and across the Andes from 27° to 55°S, including some sites with hourly data. Along the Pacific (west) coast, AR landfalls are most frequent between 38° and 50°S, averaging 35–40 days yr^{-1}. This decreases rapidly to the south and north of this maximum, as well as to the east of the Andes. Landfalling ARs are more frequent in winter/spring (summer/fall) to the north (south) of ~43°S. ARs contribute 45%–60% of the annual precipitation in subtropical Chile (37°–32°S) and 40%–55% along the midlatitude west coast (37°–47°S). These values significantly exceed those in western North America, likely due to the Andes being taller. In subtropical and midlatitude regions, roughly half of all events with top-quartile precipitation rates occur under AR conditions. Median daily and hourly precipitation in ARs is 2–3 times that of other storms. The results of this study extend knowledge of the key roles of ARs on precipitation, weather, and climate in the South American region. They enable comparisons with other areas globally, provide context for specific events, and support local nowcasting and forecasting.

1. Introduction

As first identified by Newell et al. (1992), atmospheric rivers (ARs) are long and narrow corridors of strong water vapor transport usually located ahead of cold fronts over the oceans. As a result, ARs are identified as synoptic-scale transient flow features linked to extratropical cyclones that tend to occur in storm tracks (Zhu and Newell 1994, 1998). Aircraft-based observations across cold fronts over the northeast Pacific, combined with new satellite measurements of vertically integrated water vapor (IWV), confirmed the filamentary structure of ARs (Ralph et al. 2004, 2005) and that a single AR can contribute to about 25% of Northern Hemisphere meridional transport. While many AR studies have focused on the water vapor transport from the oceans to the continents from an Eulerian framework, looking at instantaneous fields of IWV or integrated vapor transport (IVT; e.g., Zhu and Newell 1998; Neiman et al. 2008; Rutz et al. 2014), other studies have described the water vapor transport ahead of the cold front in a Lagrangian framework as occurring within a coherent, warm stream that ascends over the warm front, referred to as the warm conveyor belt (e.g., Browning 1990; Eckhardt et al. 2004). Both features, in fact, represent two ways to describe water vapor transport associated with baroclinic waves that may be related such that moist air parcels moving through an AR ascend over the warm frontal zone within a warm conveyor belt (e.g., Sodemann and Stohl 2013).

Water vapor transport in ARs is emerging as a global science topic, and the role of ARs in producing floods

Corresponding author: Maximiliano Viale, maxiviale@mendoza-conicet.gob.ar

DOI: 10.1175/JHM-D-18-0006.1

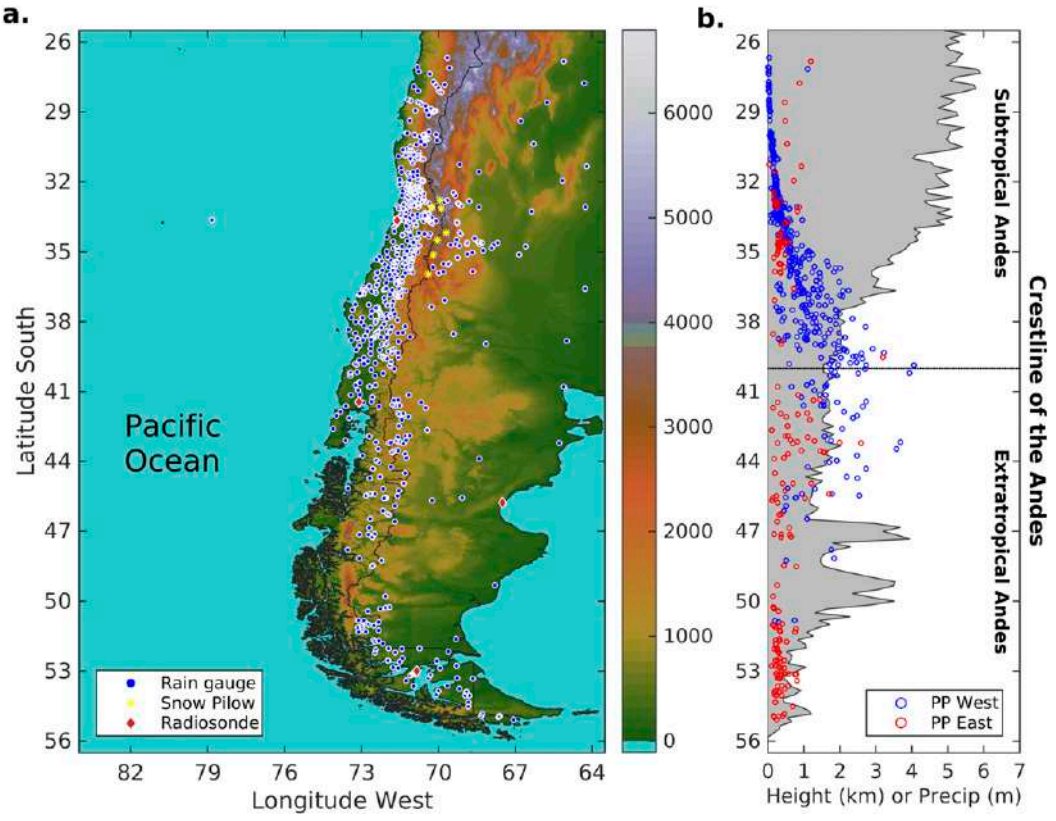

FIG. 1. (a) The study region over southern South America with the locations of daily rain gauges used (blue circles), snow pillow sensors (yellow asterisks), and the radiosonde (red diamonds) datasets. The topographic map is included and color coded (m), and the Argentina–Chile border is plotted since it approximately represents the crest line of the Andes. (b) The crest line of the South American Andes (km) and the annual mean precipitation (m) at station sites are plotted as a function of latitude. The height of the crest has been smoothed for an effective visualization, while the sites located west and east of the divide have been plotted in red and blue, respectively.

and providing water resources is being increasingly demonstrated around the world (Ralph et al. 2017a). When ARs impact mountainous coastal regions, they can produce heavy orographic precipitation, making a valuable contribution to the regional water balance but also setting the stage for hydrometeorological hazards. On the west coast of North America, where these systems have been widely studied, ARs contribute to about 30%–50% of the annual precipitation (Guan et al. 2010; Dettinger et al. 2011; Ralph et al. 2013; Rutz et al. 2014) and make a large contribution to extreme precipitation (Ralph et al. 2006; Neiman et al. 2011; Ralph and Dettinger 2012; Warner et al. 2012; Lamjiri et al. 2017). Similar contributions of the AR storms to the wet (winter) season total precipitation and extreme events have been recently documented in South Africa (Blamey et al. 2018) and for all seasons in western Europe and the central United States (Lavers and Villarini 2015; Ramos et al. 2015).

South of about 30°S, precipitation along the western side of South America is mainly produced by frontal systems associated with midlatitude cyclones (e.g., Falvey and Garreaud 2007). These storms make frequent landfall, mostly in winter in the subtropics (30°–40°S) and throughout the year in the extratropics (40°–55°S; e.g., Garreaud 2009), leading to a large north–south gradient in annual precipitation and numbers of rainy days (Fig. 1b). Superimposed on this north–south precipitation gradient are marked west–east variations produced by the effects of the high Andes Cordillera (e.g., Falvey and Garreaud 2007; Viale and Nuñez 2011; Viale and Garreaud 2015) that runs continuously with its crest about 200 km from the Pacific coast (Fig. 1a). Consistent with its proximity to the vast South Pacific Ocean and the prominent topography, the west coast of South America should be deeply impacted by ARs. Indeed, a few studies have documented landfalling ARs and orographic precipitation processes in the subtropical sector of this region (Viale and Nuñez 2011; Garreaud 2013; Viale et al. 2013). Nonetheless, an objective and spatially complete AR characterization reaching the entire

southwestern coast of South America is lacking. Likewise, an assessment of the AR contribution to the mean precipitation and extreme events is missing.

Motivated by the aforementioned research gaps, in this work we present a comprehensive examination of the impact of ARs on precipitation in southern South America, with an emphasis on the west coast and the Andes Cordillera. This climatological study is important for several reasons. First, it provides a basis to analyze past or future individual AR events, especially those associated with extreme precipitation events. The later events often result in flooding and landslides with dramatic consequences on society (e.g., Garreaud and Rutllant 1996; Viale and Norte 2009). Along the same lines, the characterization of ARs and their impact on precipitation (annual accumulation and extreme events) may be useful for precipitation forecast guidance. Finally, our climatology of ARs in southern South America will be compared with those obtained along the west coast of North America, an area that shares many geographical similarities with the region studied here, but also exhibits some differences, adding further diversity to the global survey of ARs.

This study uses 16 years of gridded reanalysis and station-based daily/hourly precipitation records. First, an automatic methodology to identify landfalling ARs over the southeast Pacific is introduced. The approach here modifies the Guan and Waliser (2015, hereafter GW15) method by adding a link to the midlatitude frontal dynamics and not considering a fixed lower limit of IVT as threshold. Second, the frequency of landfalling ARs and some of their features from the southern tip of the continent to subtropical latitudes are examined. Finally, the role of ARs in providing water resources to the region and in producing intense precipitation is documented.

2. Data and methodology

a. Reanalysis and surface precipitation data

The analyses are based on three main datasets: the Climate Forecast System Reanalysis (CFSR), meteorological soundings, and surface precipitation observations. The CFSR data are used to detect AR conditions (section 2b), while surface observations are employed to evaluate their hydrometeorological impacts. CFSR data belong to the last generation of the available global reanalysis, generated by a coupled atmosphere–ocean–land surface–sea ice system (Saha et al. 2014). Six-hourly surface- and pressure-level fields are available on a 0.5° × 0.5° latitude–longitude grid. CFSR gridded data over the 10°N–60°S and 180°–35°W domain were employed to calculate IVT from 2001 to 2016. IVT was used to determine AR conditions by applying an algorithm that is explained below. To calculate the IVT vector at each grid cell, the following formula was used:

$$\mathrm{IVT} = \frac{1}{g}\int_{p_{\mathrm{sfc}}}^{100\mathrm{hPa}} q\mathbf{V}\,dp\,, \tag{1}$$

where $\mathbf{V} = (u, v)$ is the horizontal wind vector determined by its meridional and zonal wind components, q is the specific humidity, p_{sfc} is the surface pressure, p is the pressure level, and g is the gravitational acceleration. The integration is done using data at the surface and 100-hPa level, which correspond to 26 vertical pressure levels available in CFSR data if the surface pressure is higher than 1000 hPa. Otherwise, the number of vertical levels used depends on the surface pressure. Given the crucial role of IVT in identifying ARs, an evaluation of the reanalysis-based IVT against radiosonde-observed IVT is provided in the appendix. Based on four radiosonde stations in southwestern South America (SA), the RMSE of IVT was about 50–100 $\mathrm{kg\,m^{-1}\,s^{-1}}$ and bias was 15–40 $\mathrm{kg\,m^{-1}\,s^{-1}}$, which represent errors of the order of 10% or less and so suggest that CFSR data are suitable for this study.

Daily and hourly rain and daily snow datasets managed by the Chilean and Argentinean agencies of water, agricultural, and weather services are used to estimate the hydrometeorological impacts of ARs. Figure 1 shows the location of the 739 stations reporting daily accumulations at 1200 UTC (0900 LT). Only time series with less than 20% missing data from 2001 to 2016 were used. In the high subtropical Andes (30°–35°S), six snow pillow sensors provide daily snow water equivalent (SWE) between 2001 and 2015 (15 years). A relatively new hourly rain dataset is available for the last 4 years (2013–16), from which hourly time series containing less than 10% missing data were used.

b. Methodology for AR detection using reanalysis-derived IVT data

The first step for AR detection is checking if the IVT magnitude surpassed a given threshold defined locally as the 85th percentile value. For each month, the 85th percentile IVT values are calculated at all grid cells using all time steps within a 5-month window (e.g., target month ± 2 months) over the period of 2001–16. The 85th percentile threshold was proposed by Lavers et al. (2012) and then used by GW15, who noted some advantages over using a fixed IVT threshold value of 250 $\mathrm{kg\,m^{-1}\,s^{-1}}$ (e.g., Rutz et al. 2014, 2015; Ralph et al. 2017b). The percentile-based threshold varies substantially in time and space, so it more fairly isolates the departure of IVT from its background state. When comparing both IVT-threshold methods (percentile and fixed value) in

determining the AR occurrences on the coast of Chile (not shown), it was found that the fixed threshold method generated more ARs on the southernmost coastal sector and fewer ARs over the interior of the continent (i.e., reduced inland penetration of ARs over the Patagonia), which seems to be not coherent with the AR climatology at similar-latitude west coast locations (e.g., west of the United Kingdom; Lavers and Villarini 2015).

The flowchart in Fig. 2 highlights the main processes of the AR detection algorithm introduced here. For a given time step, the algorithm starts checking the IVT criterion at grid cells along the 76°W meridian (just to the west of coastline of Chile). If a column of contiguous grid cells meets the IVT criterion, then the successive north–south grid columns to the west and to the east of the initial column are inspected to isolate a contiguous region (henceforth referred to as an ''object'') that verifies the IVT criterion. The east and west boundaries of this object of enhanced IVT are determined by three requirements: first, the mean IVT direction of the new, subsequent east or west columns of the object must be between 270° and 360° (i.e., northwest direction) and not change more than 45° with respect to the mean IVT direction of the object established up to this step. This requirement intends to guarantee the poleward transport of moisture during pre-cold-frontal conditions and to maintain a coherence of the IVT direction in the object. Second, because the successive locations of the IVT maximum will form the axis of the object, the location of the maximum IVT magnitude in the subsequent east or west columns must be less than 3° latitude apart from their location in the previous column of the object. Third, the length of the new columns must not be 250% larger or 20% shorter than the length of the previous column, and both contiguous columns must share at least 15% of their grid cells at the same latitudes to avoid a sharply curved object. The percentages for the allowed expansion (250%) or reduction (20%) of the new adjacent column length represent the 75th percentile values of all expansion or reduction change between successive columns.

Once an object of enhanced IVT is isolated, further requirements of its landfall, narrowness, and its association with a frontal zone are checked. The object makes landfall if at least one of its axis grid cells overlaps with the land mask of the CFSR reanalysis. Then, its length is calculated as the summation of the Earth surface distance between successive axis grid cell locations, which in turn must be greater than 2000 km (1500 km) south (north) of 35°S, and the ratio of the Earth surface area of the object to its length (representative of its width) must be greater than 2. This ratio represents the criterion of a plume of IWV longer than 2000 km and narrower than 1000 km, which was established by Ralph et al. (2004) and widely used in

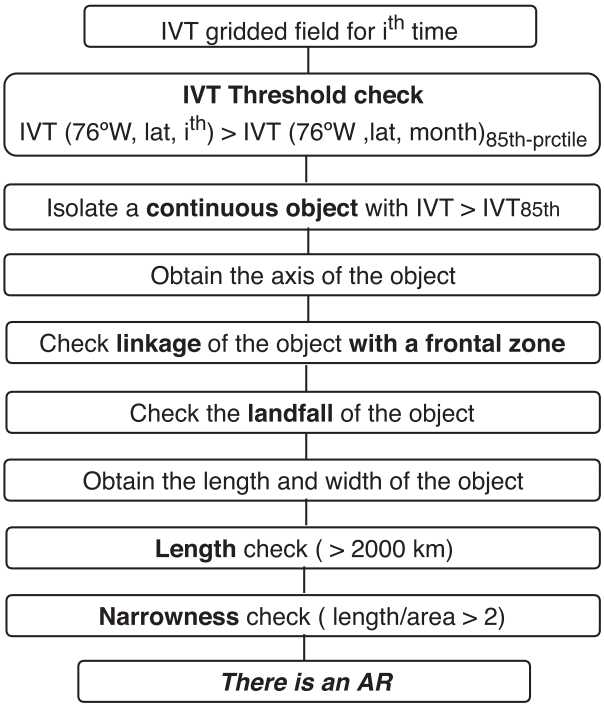

FIG. 2. Flowchart of the main processes of the AR detection algorithm applied to a 6-hourly gridded IVT field derived from the reanalysis CFSR dataset over the 2001–16 period.

subsequent works. Since the recent definition in American Meteorological Society's *Glossary of Meteorology* links ARs with cold fronts and midlatitude cyclones (Ralph et al. 2018), the algorithm introduced here also requires that the object must be associated with a near-surface frontal zone. By using the 1000–850-hPa thickness from the CFSR data, frontal zones are identified as areas where the magnitude of the horizontal gradient of the thickness exceeds 5 m (100 km)$^{-1}$. This value is close to that used by Jenker et al. (2010) to detect fronts in a high-resolution reanalysis. The near-surface frontal zone is searched only over the ocean, to the west of the 76°W reference meridian, because of the strong disruption of near-surface fronts by the Andes Mountains. An object is then associated with a frontal zone if its area intercepts or is located immediately north (up to ~50 km apart, i.e., one grid cell of separation) of the area of the frontal zone. If the object is linked to a frontal zone then it is tagged as an AR for this specific time step.

From a total of 23 376 six-hourly time steps between 2001 and 2016, 10 812 (~46%) time steps were initially identified as enhanced IVT objects by the algorithm in the southeast Pacific, and 3486 (~15%) objects were finally classified as landfalling ARs. Of the remaining 7326 objects not classified as ARs, 2927 (~40%) did not make landfall, 3159 (~43%) did not stretch longer than the thresholds, 11 (~0.1%) did not meet the narrowness

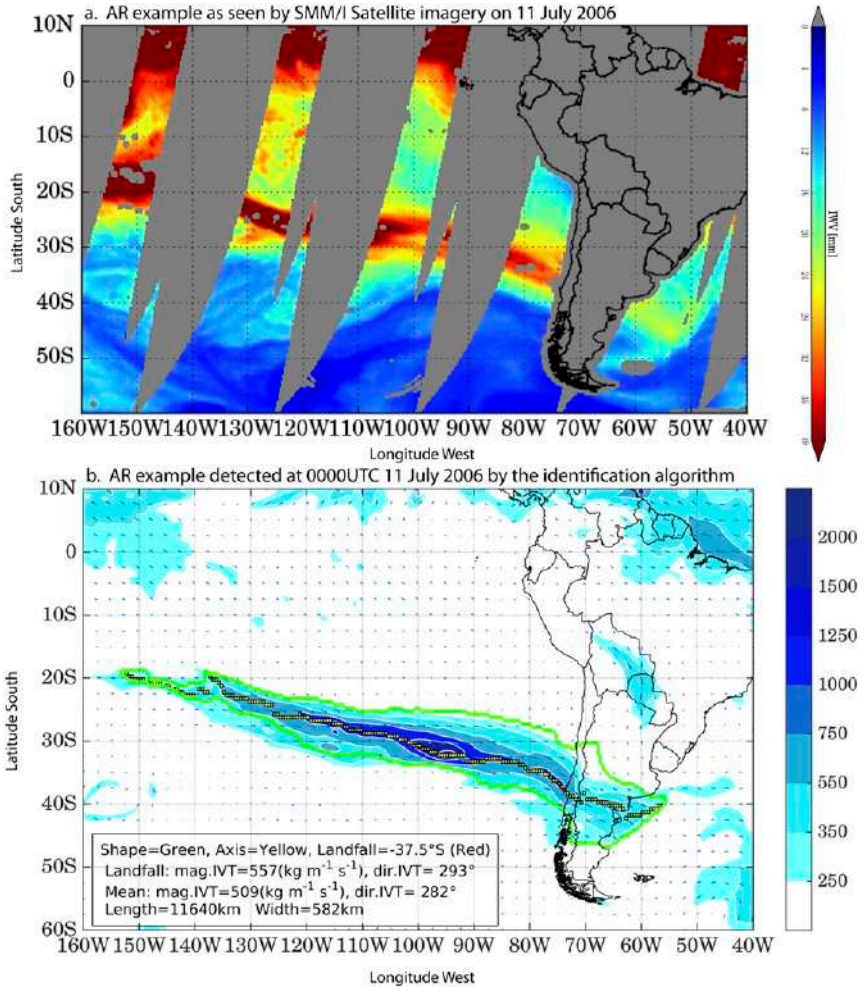

FIG. 3. (a) Chart of the IWV (mm) as seen by the SMM/I satellite imagery during the morning passes on 11 Jul 2006 showing an AR example. (b) Chart of the IVT ($kg\,m^{-1}\,s^{-1}$) magnitude and direction (color shading and vectors, respectively) showing the AR example detected at 0000 UTC 11 Jul 2006 by the algorithm. The algorithm outputs of the shape boundary (green), axis (yellow), landfall location (red), and other key metrics are shown in the bottom-left corner. This case was one of the most devastating ARs over the period of 2001–16.

criterion, 693 (~9%) did not have poleward water vapor transport, and 536 (~7%) were not linked to a frontal zone. These statistics demonstrate that most of the long plumes of enhanced IVT are narrow and linked to a frontal zone. Linking the object to a near-surface frontal zone and not considering a fixed lower limit of IVT ($100\,kg\,m^{-1}\,s^{-1}$) as a threshold are the two main differences with the GW15 method for detecting ARs. In our method, the first difference helps to filter out false-alarm ARs over the dry subtropical west coast of SA (north of 25°S) where cold fronts hardly ever arrive (e.g., Seluchi et al. 2006), and IVT plumes are mostly associated with midlevel cutoff low pressure systems instead. The second difference allows us to detect AR conditions over the high subtropical Andes and the dry subtropical west coast (35°–25°S), where the 85th percentile value of IVT is lower than $100\,kg\,m^{-1}\,s^{-1}$ due to the normal extremely dry conditions there.

An example of an AR observed by the SSM/I satellite imagery and the key outputs from the AR detection algorithm are shown in Fig. 3. It includes several features of the AR, such as the shape boundary (green), axis (yellow), landfall location (red), IVT direction and magnitude at the landfall location, the mean IVT direction and magnitude, and the length and width of the AR. The AR shape boundary in all time steps when ARs were detected is used to estimate the frequency and precipitation contributions of landfalling ARs. It is worth noting that the AR in Fig. 3 was one of the strongest ARs in the period studied. Also, this AR was associated with extreme precipitation, floods, and

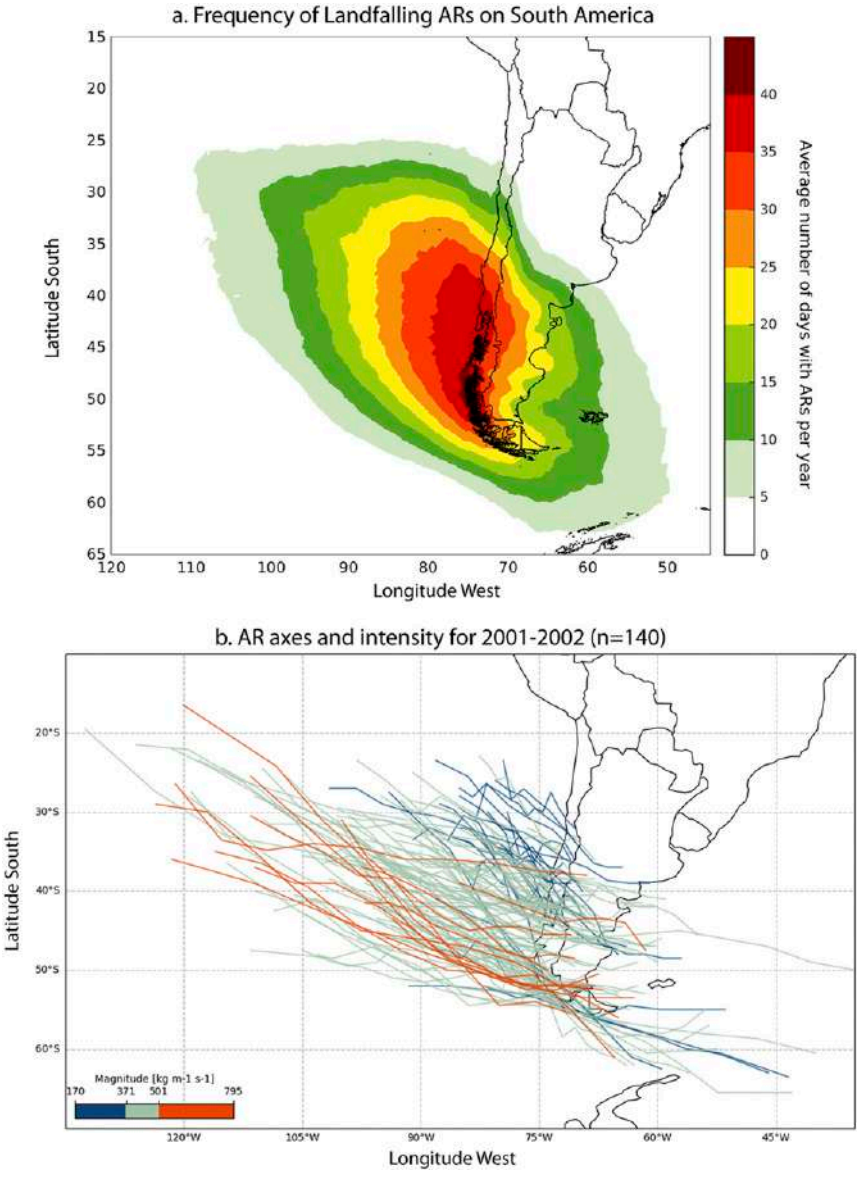

FIG. 4. (a) Annual frequency (average number of days with ARs per year) of landfalling ARs on South America for the 2001–16 period. (b) Spaghetti plot showing only the axes for the 140 ARs at the first time when they made landfall between 2001 and 2002 (2 years). The mean IVT magnitude of each AR is colored as a weak (blue, below the 25% percentile value), moderate (green, between the 25% and 75% percentile values), or strong (red, above the 75% percentile value) case for all landfalling ARs for the 2001–16 climatology.

fatalities in central Chile (e.g., Garreaud 2013) and coincided with a severe downslope windstorm in central-western Argentina (e.g., Norte et al. 2008).

3. Climatology of landfalling ARs on the west coast of South America

This section employs the reanalysis database of landfalling ARs, which includes 3486 time steps under AR conditions (2001–16), to illuminate their main features. Note that the analysis only represents those ARs that, at some moment of their life cycle, made landfall along the west coast of South America. The AR frequency was calculated as the average number of days per year meeting the AR identification criteria (Fig. 4a). At least one of the four reanalysis times per day (6-h IVT analysis) must meet the AR identification criteria to be considered as a day with AR conditions. ARs make

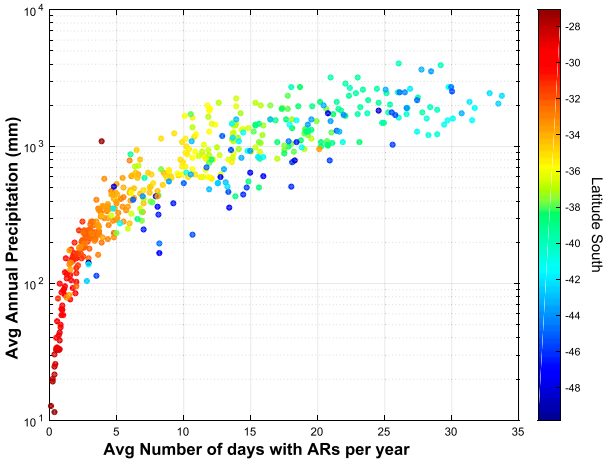

FIG. 5. Scatterplot of the average number of days with ARs per year and the annual mean precipitation (log scale) at each surface precipitation station on the windward side of the Andes for the 2001–16 period. The station latitude is color coded.

landfall all along the west coast from 25°S to the southern tip of the continent (about 3000 km in length), but most frequently (35–40 days per year) between 38° and 52°S and with an absolute maximum of 40–45 days at ~48°S. The AR frequency along the coast and offshore decreases rapidly to the south of 51°S and to the north of 35°S. The frequency of time in which a landfalling AR affected the interior of the continent decreased sharply to the east of the Andes, especially at subtropical latitudes where the mountains are high (Fig. 1b). Figure 4b shows the axes of 140 ARs during only landfall time between 2001 and 2002 to illustrate further details of AR behavior. Stronger and longer landfalling ARs tend to occur farther south of the west coast, and their northwestward extension over the Pacific Ocean rarely surpasses ~5000 km in length and reaches the 20°S latitude line.

As shown in Fig. 5, the increase of AR frequency with respect to latitude is generally associated with higher annual mean precipitation at windward-side surface precipitation stations, although the logarithmic relationship degrades as the AR frequency increases, likely due to orographic influences on precipitation, as discussed below.

The seasonality of the AR frequency is shown in Fig. 6. The occurrence of ARs maximizes along the coast to the south of Chiloe Island (~43°S) in summer and fall (Figs. 6a,b) and to the north of Chiloe in winter and spring (Figs. 6c,d). Since the occurrence of precipitation gradually focused on one season (winter) equatorward along the southwest coast of SA (Viale and Garreaud 2015), it is likely that ARs more strongly modulate precipitation in the subtropics than in the extratropics. As discussed later, our results for AR seasonality in SA

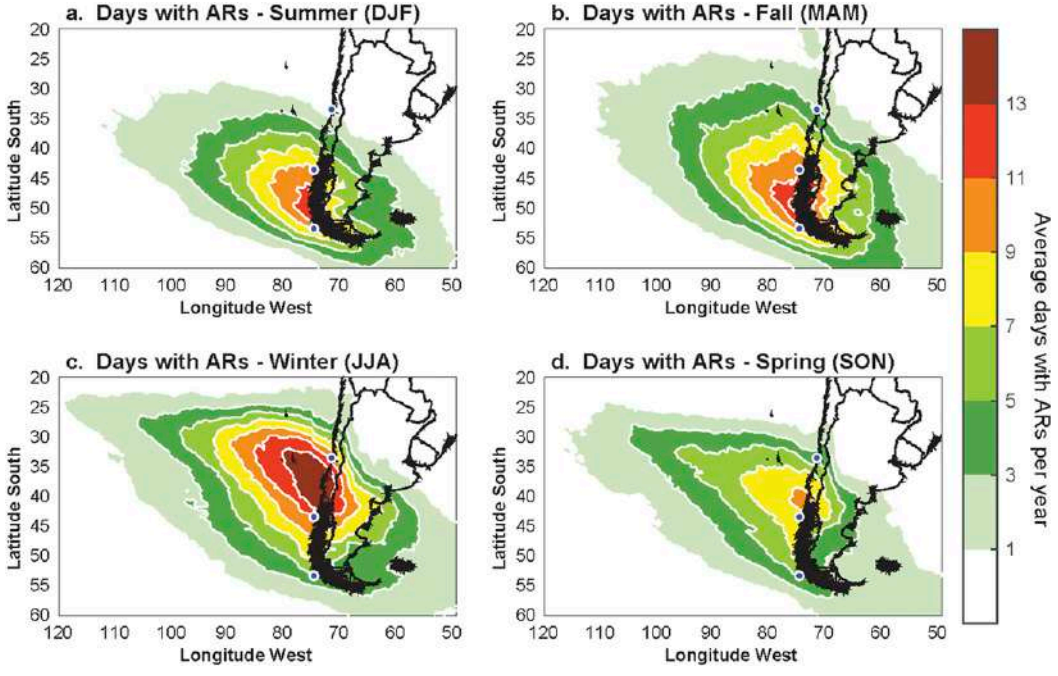

FIG. 6. Seasonal frequencies (average number of days with ARs per year) of landfalling ARs on the west coast of South America: (a) summer (DJF), (b) fall (MAM), (c) winter (JJA), and (d) spring (SON). Blue points are plotted on the coast for reference at 33.5°S (latitude of Santiago), 43.5°S (southern Chiloe Island), and 53.5°S (latitude of Punta Arenas).

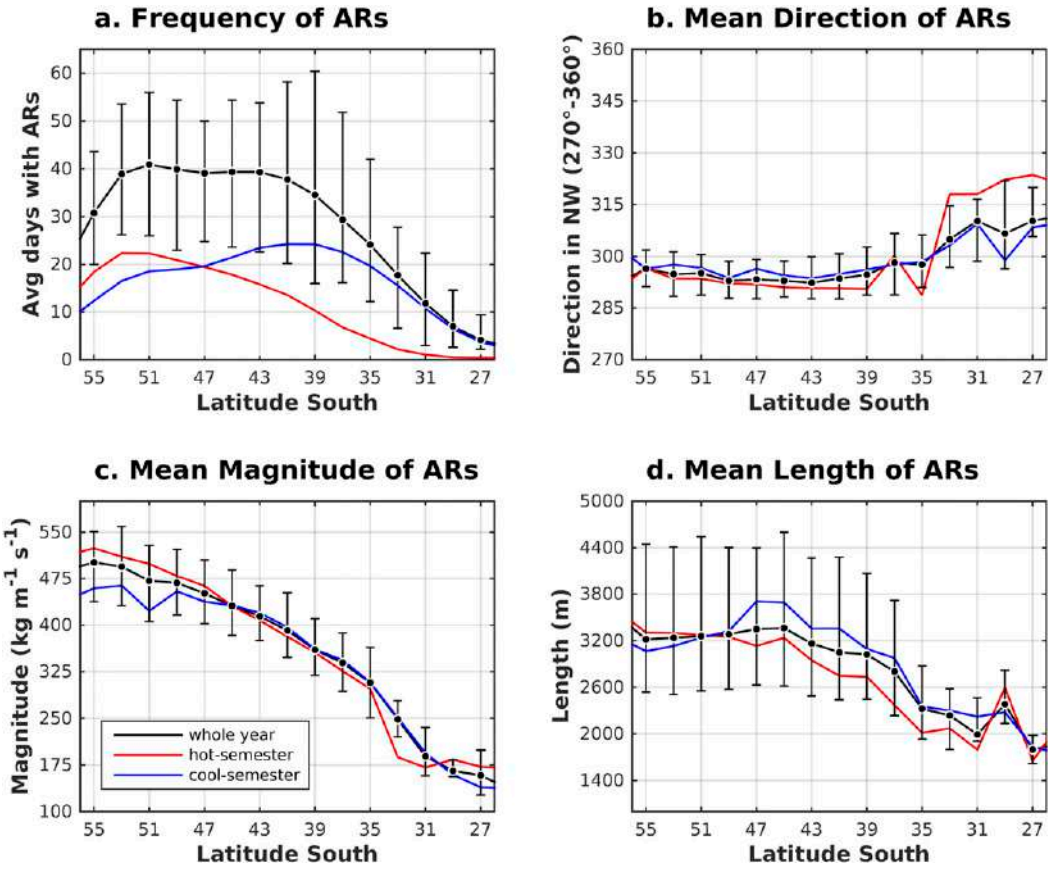

FIG. 7. Features of landfalling ARs for the whole year (black) and the warm (October–March in red) and cold (April–September in blue) semesters as a function of latitude: (a) frequency, (b) mean direction, (c) mean magnitude, and (d) mean length of landfalling ARs. The series represent the mean value of metrics calculated by using 6-hourly CFSR data over the 2001–16 period for landfalling ARs and within 2° latitude bands. For the whole year series, the mean and interquartile range (25th and 75th percentile) within each 2° latitude band are also presented.

are in close agreement with those from previous studies over the west coast of North America (e.g., Neiman et al. 2008).

Additional features of landfalling ARs for the whole year and the warm (October–March) and cool (April–September) semesters are presented as a function of latitude in Fig. 7 by selected metrics calculated within 2° latitude bands. Further evidence of higher AR frequencies to the south (or north) of ~43°S for summer (winter) is shown in Fig. 7a. The interquartile range of frequency for the whole year (shown by error bars) denotes a relatively large interannual variation in AR occurrence in the extratropics (south of 35°S). For other AR features (Figs. 7b,c), the variations along the coast are gradual and change little for different seasons. The horizontal water vapor transport associated with ARs is more intense and longer but less poleward oriented in the extratropics than in the subtropics regardless of the season, which could be explained by the preferential extratropical track of the cyclone centers (e.g., Hoskins and Hodges 2005) and the accentuated blocking effect of the high subtropical Andes on the water vapor transport and airflow (e.g., Viale et al. 2013).

4. Impact of ARs on precipitation

a. Contribution of ARs to total annual precipitation

This section examines the contribution of ARs to total precipitation using daily station records. Consider a given station with daily precipitation (measured at 1200 UTC) on 17 July 2006. To determine if the precipitation should be counted as AR related, the first step is to search for AR conditions at the four grid points that enclose the station site between 1200 UTC 16 July and 1200 UTC 17 July. If AR conditions were present at any of the four grid points at any of the five CFSR times, that day is labeled as an AR-precipitation event. The precipitation in the next day (18 July, if any) is also linked to the AR. Including the day after the AR occurrence was

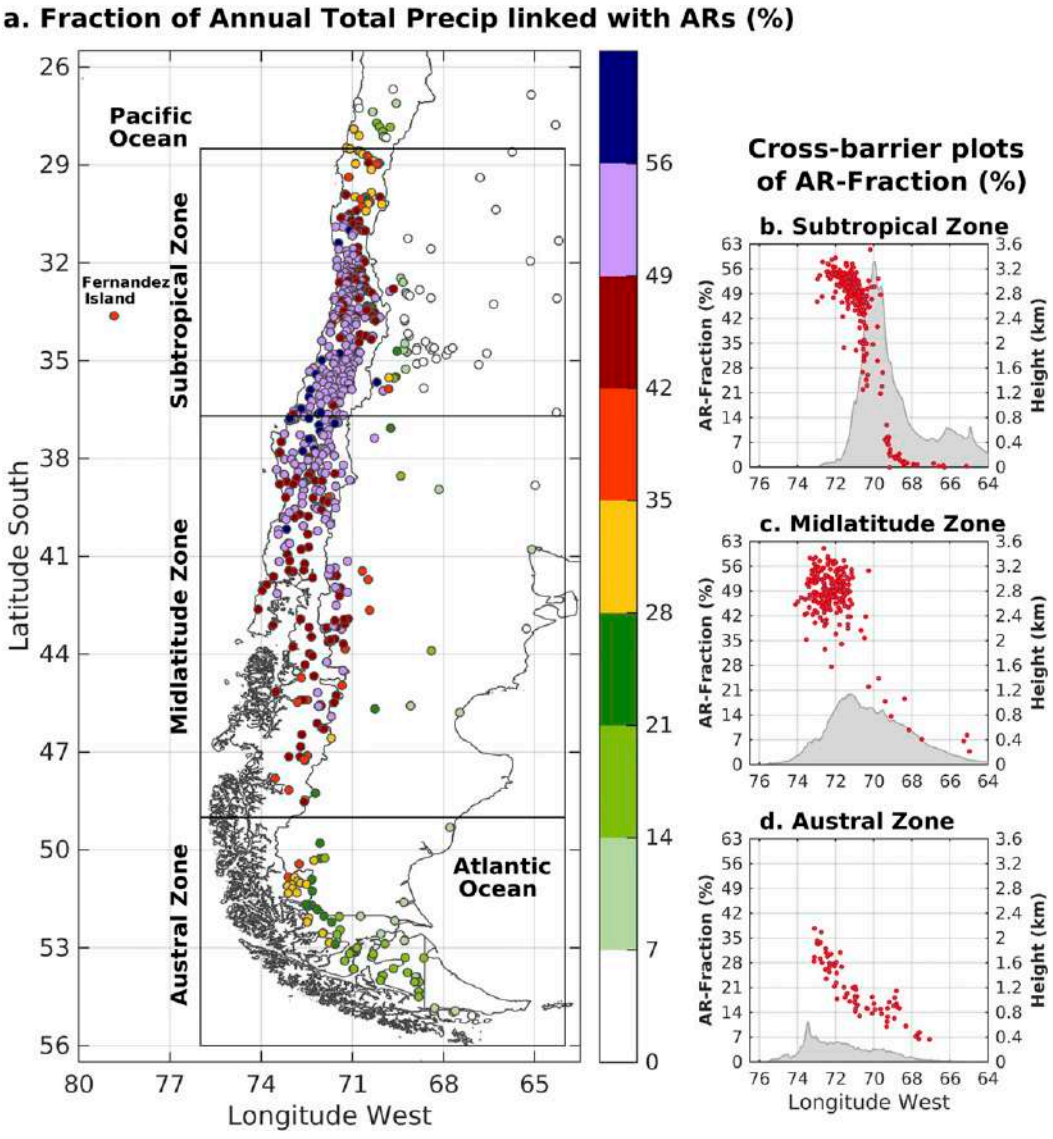

FIG. 8. (a) Fraction of annual total precipitation associated with AR conditions over the 2001–16 period. Fractions are multiplied by 100 to express the results in percentage. AR fractions at each station site are calculated using daily rain datasets. Cross-barrier plots of the AR fraction for the (b) subtropical, (c) midlatitude, and (d) austral zones. The limits of each zone are defined in the plan-view plot of (a). The meridionally averaged west–east cross sections of the topography [within the rectangle shown in (a)] are shown in (b)–(d) as a reference.

also considered in previous studies (e.g., Dettinger et al. 2011; Rutz et al. 2014) to take into account delayed times between the AR conditions and the measurement of precipitation accumulation at the surface gauges. The total contribution of ARs to the total annual precipitation at each station (Fig. 8) was determined by summing the precipitation during all AR-precipitation events.

The contribution of ARs to the annual total precipitation is largest along the subtropical west coast, with values between 49% and 63%. This contribution reduces markedly to the north of 32°S (<8% at windward-side stations) due to the sharp reduction in AR occurrence (Fig. 4). To the east of the subtropical Andes (roughly delimited by the Chile–Argentina border; Figs. 8a,b) ARs are rather infrequent and have a small contribution to total precipitation (less than 15%). In midlatitudes (39°–49°S), the AR contribution to the total precipitation is still large (42%–56%) both along the coast and even in some stations immediately to the east of the Andes crest (Figs. 8a,c). Farther east the AR contribution decreases down to less than 10% near the Atlantic sea border, despite a moderate AR frequency

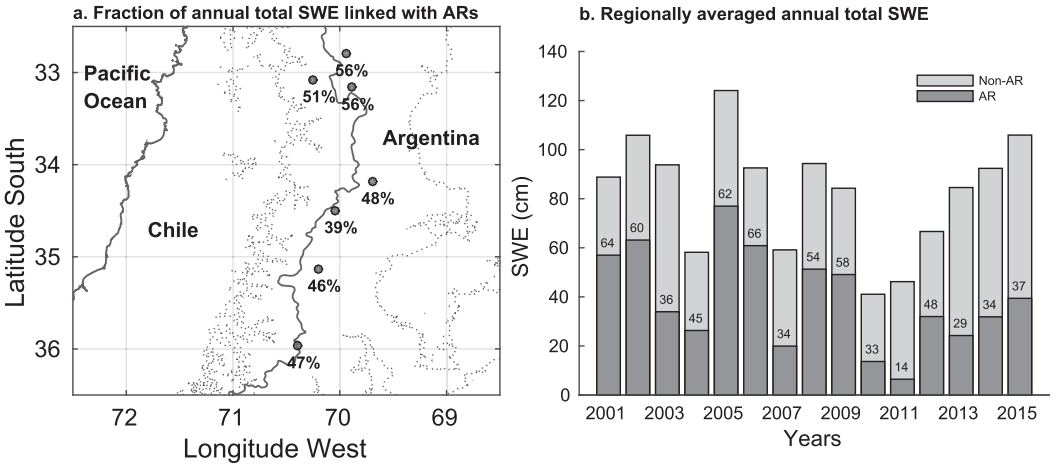

FIG. 9. (a) Fraction of snow total precipitation associated with ARs at snow pillow locations over the 2001–15 period. Fractions are multiplied by 100 to express the results in percentage. The topographic line of 1500 m (dotted line) and the Argentina–Chile border line (solid line) are plotted as references. (b) Regionally averaged annual contribution of ARs to total annual snow over the 2001–15 period, calculated using the seven SWE sites shown in (a). The numbers within each bar correspond to the percentage of the annual contribution of ARs to total annual snow for each year.

(Fig. 4). South of 47°S nearly all the stations are located to the east of the austral Andes, but the AR contribution ranges from 40% for stations immediately to the lee to less than 15% for stations farther east close to the Atlantic coast (Figs. 8a,d). In comparison with previous studies in the west coast of North America (Dettinger et al. 2011; Rutz et al. 2014), the percentages of AR contribution to total precipitation in South America are quite similar, except for the central Chile region where they are slightly higher, which could be attributed to different methodology and a stronger orographic effect as discussed below. The regional-averaged annual contribution of ARs for the subtropical, extratropical, and austral zones was calculated using stations enclosed by rectangles in Fig. 8a. The mean values for the entire 16-yr period were 46%, 46%, and 23%, respectively, while the lowest and highest yearly values ranged from 23% to 67%, from 28% to 63%, and from 14% to 30% in each subregion.

A few snow pillow stations available in the high subtropical Andes (30°–36°S) allow estimation of the contribution of AR storms to the annual snowpack accumulation. This variable is of crucial relevance for agriculture in central Chile and central-western Argentina, as snowmelt provides the much-needed water during summer months. To attribute daily SWE to ARs, the same criterion used for rain gauges is applied to the SWE sites. As in low areas on the windward side of the Andes, the AR storms contributed largely (38%–56%) to total annual snowpack at the mountain sites (Fig. 9a), with the highest percentages (~56%) at the northernmost sites (around 33°S). The regionally average annual contribution of ARs, calculated using the seven SWE sites, ranged from 14% in 2011 to 66% in 2006 and averaged ~55% in the 15-yr period (Fig. 9b). For comparison, Guan et al. (2010) found roughly 40% contribution from ARs to Sierra Nevada precipitation in California, which is somewhat less than is found here for the Andes.

b. *Impact of ARs on precipitation intensity*

As highlighted in the introduction, landfalling AR storms often lead to heavy precipitation events, especially on mountainous coastal regions where orographic effects largely enhance precipitation, causing floods and landslides. The west coast of SA is such a place where the impact of ARs against the long, high Andes leads to heavy orographic precipitation events (e.g., Viale and Nuñez 2011; Viale et al. 2013; Garreaud 2013).

To compare precipitation intensity under AR and non-AR conditions, the median daily precipitation is calculated separately for days with and without AR conditions at each station and then the ratio between them is obtained. This ratio is analogous to the normalized precipitation fraction used by Neiman et al. (2008) for similar purposes in the western United States. The ratios for the whole year and for different regions are presented in Fig. 10. AR storms produced between 1.5 and 3.5 times more daily precipitation than non-AR storms on the subtropical and midlatitudes regions on the windward side of the Andes (Figs. 10a,c,d), which coincides with the region of major AR contribution to

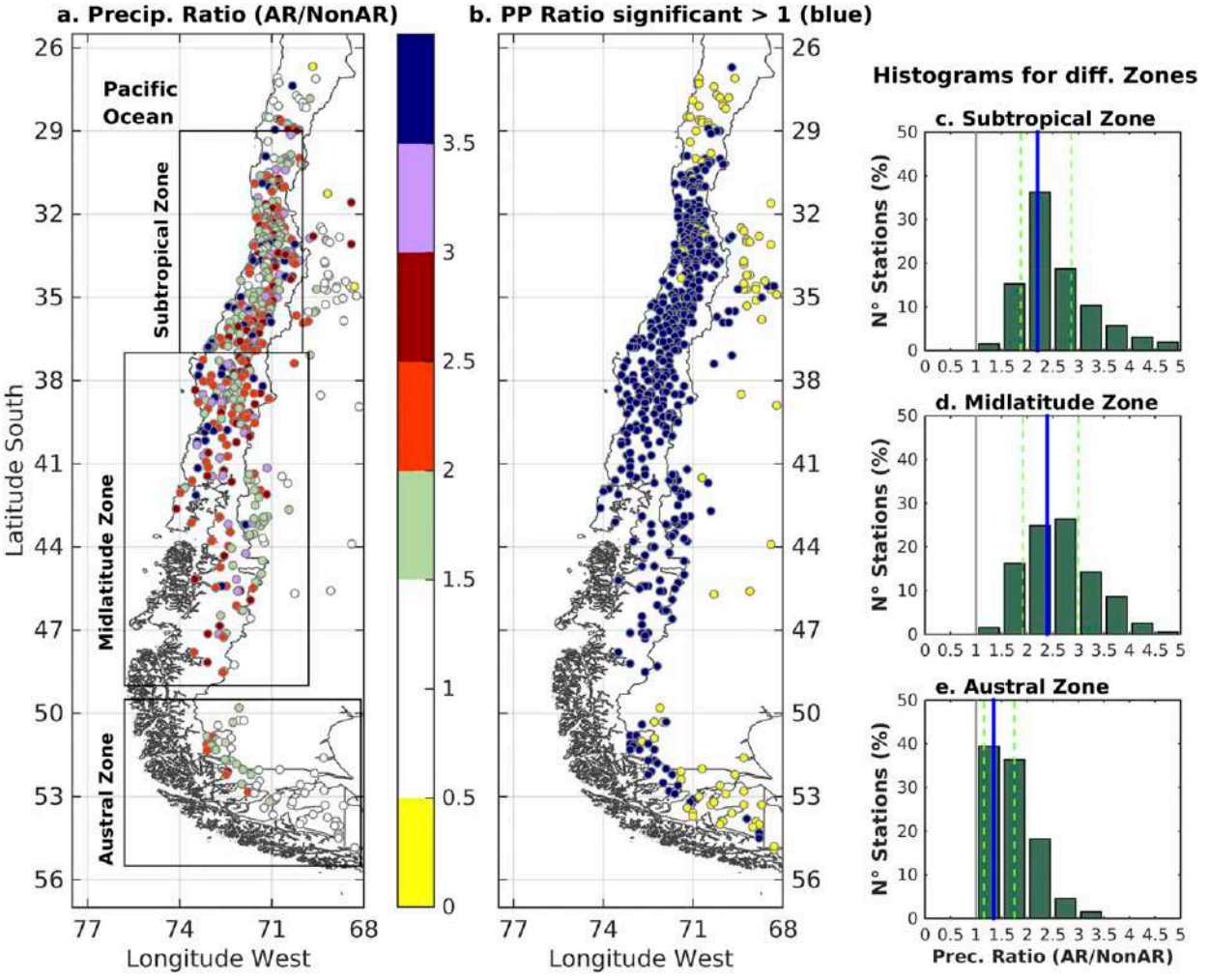

FIG. 10. (a) Ratio of the median of daily precipitation under AR conditions to those under non-AR conditions for the entire years of the 2001–16 period. Histograms showing the distribution of the same ratio at each rain gauge site grouped in different zones: (b) subtropical, (c) midlatitude, and (d) austral zones. The limits of each zone are defined in the plan-view plot in (a). The solid blue line and the dashed green lines indicate the median and the interquartile range, respectively. The solid gray line indicates the value of the ratio equal to 1, which determines the border between the intensification and decline of daily precipitation under ARs with respect to non-AR conditions.

the annual precipitation (Fig. 8). In the austral sector (Figs. 10a,e), the stations are located just east of high southern ice field or farther east in the lee, and so the ratios reduce to less than 1.5. For all the stations located upwind (Chile) and immediately east of the Andes crest, the ratios are significantly greater than 1 according to a two-sample bootstrap test (blue dots in Fig. 10b; Wilks 2011), results that denote the strong impact of ARs on daily precipitation there. Daily precipitation under AR conditions remains higher than those under non-AR conditions in both winter and summer (not shown), although this intensification is slightly larger in winter than in summer on the extratropical west coast, which agrees with the results in the western United States. (Neiman et al. 2008).

The connection of ARs with the most intense rainy days is explored by considering those days within the fourth quartile of the 2001–16 time series. Figure 11 shows the fraction of those intense rainy days associated with AR conditions at each station and in selected subregions. In the subtropical and midlatitude zones, 50%–70% of the intense rainy days occurred under AR conditions. In contrast, AR-related intense precipitation days are much less frequent in the austral zone and farther east away from the Andes.

Hourly precipitation rates under AR and non-AR conditions are compared in southwestern South America. Figure 12 shows the median and interquartile range for each of the subsets. Six hours before and after the CFSR time that met AR conditions at the four grid points that

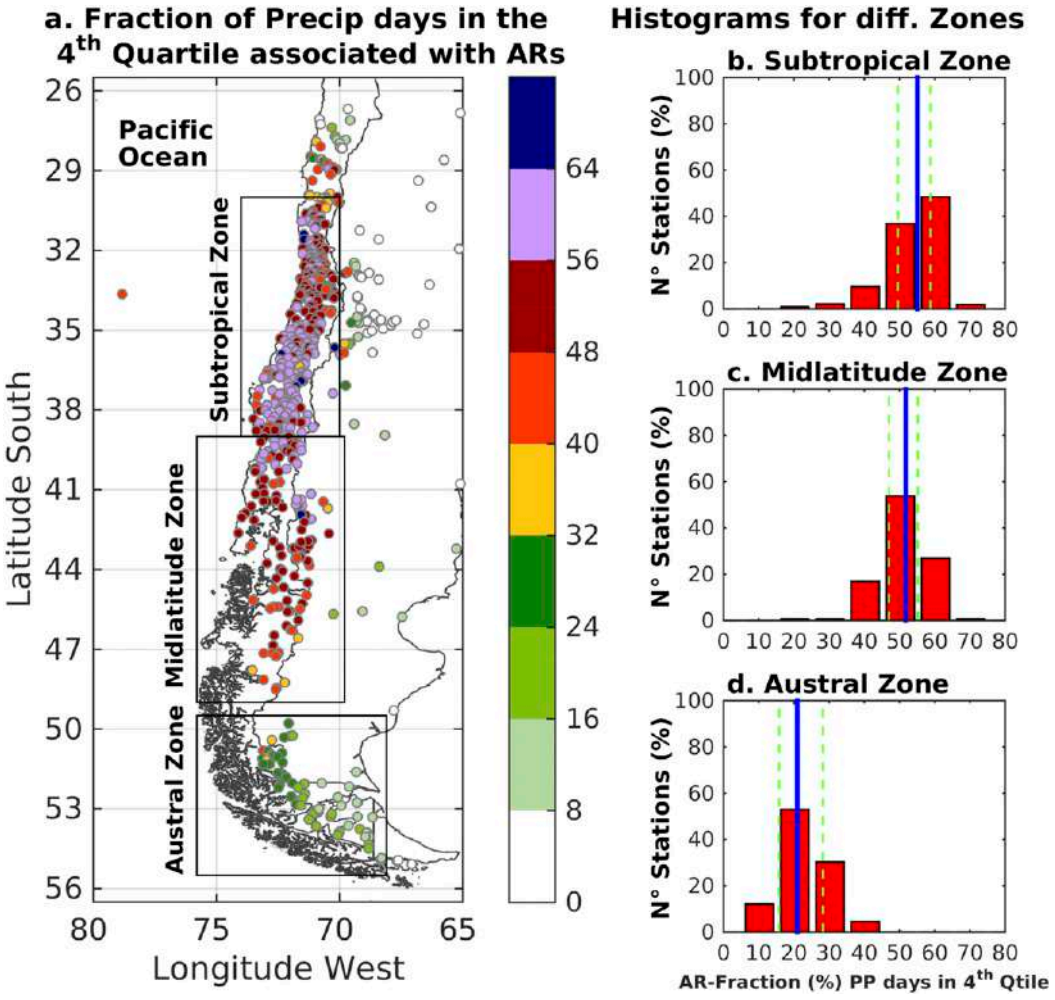

FIG. 11. (a) Fraction of daily precipitation within the fourth quartile of the total time series that is associated with AR conditions. Fractions are multiplied by 100 to be presented in percent. Histograms showing the distribution of the same fractions for stations located within different subzones [determined by the rectangles in (a)]: (b) subtropical, (c) midlatitude, and (d) austral zones. The solid blue line and the dashed green lines in (b)–(d) indicate the median and the interquartile range, respectively.

surround the rain gauge site were considered as AR rainy hours, while the remaining rainy hours were consider as non-AR. Note that both in AR and non-AR hours there is an increase in the median precipitation rates and in the variability of rates from the extratropics to subtropics (Figs. 12a,b). This signature may result from an enhanced orographic influence where the Andes are higher. For AR rainy hours, this equatorward increase in precipitation rates is larger and the 50th and 75th percentiles are double their counterparts during non-AR rainy hours (cf. Figs. 12a and 12b). The ratio of median hourly rates in the AR to non-AR subset shown in Fig. 12c (blue dots) highlights the higher hourly precipitation rates during AR hours. Nonetheless, when comparing the hourly precipitation of each subset that is within the fourth quartile of the whole 2013–16 time series, the ratio of median hourly precipitation rates (AR- versus non-AR-related intense precipitation) indicates they are more similar regardless of the AR or non-AR conditions (Fig. 12c, yellow dots).

5. Discussion and conclusions

In this study, the impact of atmospheric rivers on precipitation over southern South America was evaluated using reanalysis and surface precipitation data. ARs that made landfall on the west coast of South America over the 2001–16 period are detected through an algorithm that uses the 6-hourly IVT gridded fields from the CFSR reanalysis. This algorithm builds on that

FIG. 12. Hourly precipitation rates recorded by Chilean surface weather stations on the windward (leeward) side of the Andes during hours with (a) non-AR and (b) AR conditions. Error bars present the median (circle) and 25th and 75th percentile values (whiskers) of each subset. (c) Ratios of median precipitation intensity (blue dots) and mean extreme precipitation intensity (yellow dots) during AR conditions to those during non-AR conditions. Heavy precipitation intensity is defined as hourly precipitation rates within the fourth quartile of each subset. The smoothed topography (km) of the Andes is added in the background for reference. The stations located on the lee side of the Andes are plotted behind the topography, which is denoted by the transparency of the area plot.

developed by GW15 by requiring enhanced IVT plumes related to near-surface frontal zones. This additional criterion filters out cases of short, midlevel plumes of water vapor transport linked with midlevel cutoff lows affecting the dry subtropical west coast (north of 25°S), where signals of cold fronts at low levels are hardly seen (Seluchi et al. 2006). Because cutoff-low cases can occur without an AR and are not strictly linked to the recent definition of ARs (Ralph et al. 2018), they are not retained as ARs in this method.

Recall that the AR climatology obtained here does not include ARs moving over the South Pacific that do not make landfall along the west coast of South America. On the windward side of the Andes, ARs make landfall more frequently between 38° and 50°S, and AR conditions maximize with 35–40 days yr^{-1}. The contribution of ARs storms to the annual total precipitation is largest (49%–63%) in the subtropical windward sector (38°–32°S) and is slightly reduced but still large (42%–56%) in the extratropical windward sector (38°–50°S). To the south of 50°S and to the north of 32°S along the west coast, the AR frequency and contribution to total precipitation decreases rapidly. To the east of the Andes, an AR can penetrate into the continent only to the south of 35°S in Patagonia, but AR conditions and their contributions to precipitation reduce to 15–20 days yr^{-1} and to less than 10%, respectively. The lack of significant AR contribution to the north of 35°S in the lee of the Andes is consistent with the fact that ARs cannot penetrate this area and extremely dry downslope windstorms occur there (e.g., Norte et al. 2008; Viale and Norte 2009; Viale and Nuñez 2011). The AR seasonality along the west coast is characterized by highest frequencies in summer and fall to the south of ~43°S and in winter and spring to the north of ~43°S. Moreover, ARs are more intense and longer but less poleward oriented in the extratropics than in the subtropics regardless of the season.

The higher intensity and longer length of ARs in the extratropics could be explained by the preferential extratropical track of the cyclone centers (e.g., Hoskins and Hodges 2005), while the more poleward-oriented ARs in the subtropics could be explained by an enhanced blocking effect of the high Andes (e.g., Viale et al. 2013). Although there are some differences between the method (e.g., IWV and fixed threshold IVT) and data (e.g., different reanalysis and satellite data) for the detection of ARs and attribution to precipitation used in previous studies in North America, the annual frequency of ARs and the seasonal variation documented here are quite similar to what occurs all along the west coast of North America (Neiman et al. 2008), as well as the large contribution of ARs to total annual rain and snowpack (e.g., Neiman et al. 2008; Guan et al. 2010; Dettinger et al. 2011, Ralph et al. 2013; Rutz et al. 2014).

It is worth noting that the largest contribution to annual precipitation by ARs occurs in subtropical central Chile (38°–32°S), despite the fact that ARs are more frequent and intense farther south. This behavior has been also observed on the west coast of North America (e.g., Dettinger et al. 2011; Rutz et al. 2014). It is plausible that both coasts, California and central Chile, are a transition zone between the wet extratropics, where many weak (non-AR) storms occur, and the dry subtropics, where the bulk of the precipitation accumulates from only a few heavy precipitation events, which in turn are linked to ARs (e.g., Viale and Nuñez 2011; Dettinger et al. 2011). Thus, the dependence of total precipitation on heavy AR storms is stronger in these transitional latitudes (i.e., from subtropical to midlatitude) than in midlatitudes. Because climate change studies suggest the subtropical and ''transitional'' latitude belt is vulnerable to expansion of subtropical subsidence and to the poleward shift of the polar front, it is important to better understand the details of ARs and precipitation in such regions.

The connection of ARs with heavy precipitation events is also demonstrated here along the entire southwest coast of South America. A similar conclusion was suggested by earlier studies (Falvey and Garreaud 2007; Viale and Nuñez 2011; Barrett et al. 2011) but for a reduced sector of the coast (36°–30°S) and through more limited data (e.g., smaller databases and a subjective method to detect ARs). On daily time scales, precipitation is about 2–2.5 times greater than those under non-AR conditions, and about 50%–70% of precipitation within the fourth quartile of the entire time series belongs to rainy days under AR conditions. On hourly time scales, precipitation rates on the windward sector of the Andes gradually increase from midlatitudes to the subtropics regardless of whether an AR is present. Nonetheless, this equatorward increase accentuates under AR conditions, with rates being twice or more as high as their counterparts under non-AR conditions. This behavior may be a response to stronger orographic effects along with potentially larger contributions of warm-rain microphysics processes to total precipitation in the subtropics (see also Viale and Garreaud 2015). Although the synoptic forcing tends to be weaker in the subtropics than midlatitudes (e.g., IVT values in Fig. 7c), orographic influences on precipitation seem to strengthen northward due to the increase of the altitude of the Andes. Additionally, a sensitivity simulation with the Andes topography reduced 50% in its altitude, for comparison to the west coast mountain ranges of North America, suggested that orographic effects during landfalling ARs in central Chile would be stronger than those observed in western North America (Viale et al. 2013). This agrees with the findings here, which show slightly higher percentages of AR contribution to total precipitation in central Chile compared to those found in western North America (Dettinger et al. 2011; Rutz et al. 2014), although differences in the methodology to identify ARs or attribute rain to ARs may also play a role, according to recent discussions in the AR science community (Shields et al. 2018).

Findings here are consistent with previous research on frontal systems accompanied with prefrontal atmospheric rivers that make landfall on the west coast of North America, Europe, and South Africa. It is well recognized that when ARs intersect a coastal region with elevated terrain, they have the potential to produce heavy orographic precipitation. This paper expands the quantitative understanding that ARs constitute an important component of weather and climate in the southern region of South America that provides plenty of the water resources every year through heavy precipitation events. However, a more comprehensive understanding of the modulation of precipitation by ARs over specific river catchments within the Andes, and thus on river discharges, will require closer examination in future studies, possibly using satellite data, in situ data, and numerical simulations.

Acknowledgments. Precipitation data were obtained from the Red Agroclimática Nacional (AGROMET), Dirección Meteorológica de Chile and Dirección General de Aguas (DGA) from Chile, and Subsecretaria de Recursos Hídricos y Servicio Meteorológico Nacional from Argentina. CFSR reanalysis data were obtained from RDA web server at rda.ucar.edu. We thank Felipe Saavedra for his help in producing Fig 3a. MV, RV, and RG were supported by FONDECYT 11151009 and 3170155 and CR2/FONDAP-15110009, respectively.

TABLE A1. Coordinates, height, and missing data for radiosonde stations used in this study over the period of 2001–16. The data used correspond to observations at 1200 and 0000 UTC for the Santo Domingo station and only at 1200 UTC for the rest of stations.

Radiosonde station name	WMO ID	Lat (°S)	Lon (°W)	Height (m)	Missing data (%)
Santo Domingo, Chile	85586	33.65	71.62	75	16
Puerto Montt, Chile	85799	41.43	73.09	85	5
Punta Arenas, Chile	85934	53.10	70.88	37	10
Comodoro Rivadavia, Argentina	87860	45.79	67.47	46	26

APPENDIX

Evaluation of Reanalysis-Derived IVT Using Sounding-Derived IVT

The water vapor transport from sounding observations is compared here with CFSR reanalyses at four sounding locations in southern SA. Most made a daily radiosonde launch at 1200 UTC, except for the Santo Domingo station, which made two launches per day (1200 and 0000 UTC; see Table A1 and red diamonds in Fig. 1a). Their data and metadata were obtained from the Integrated Global Radiosonde Archive (IGRA) dataset (Durre et al. 2006). As with the IVT calculation used in the reanalysis, the IVT calculation with soundings integrates all vertical levels available between the surface and 100-hPa level. The three Chilean stations were more important because they cover the west coast from the subtropics to the southern tip of the continent. All available radiosonde observations between 2001 and 2016 were used, and the missing data percentage varies from 5% to 26%.

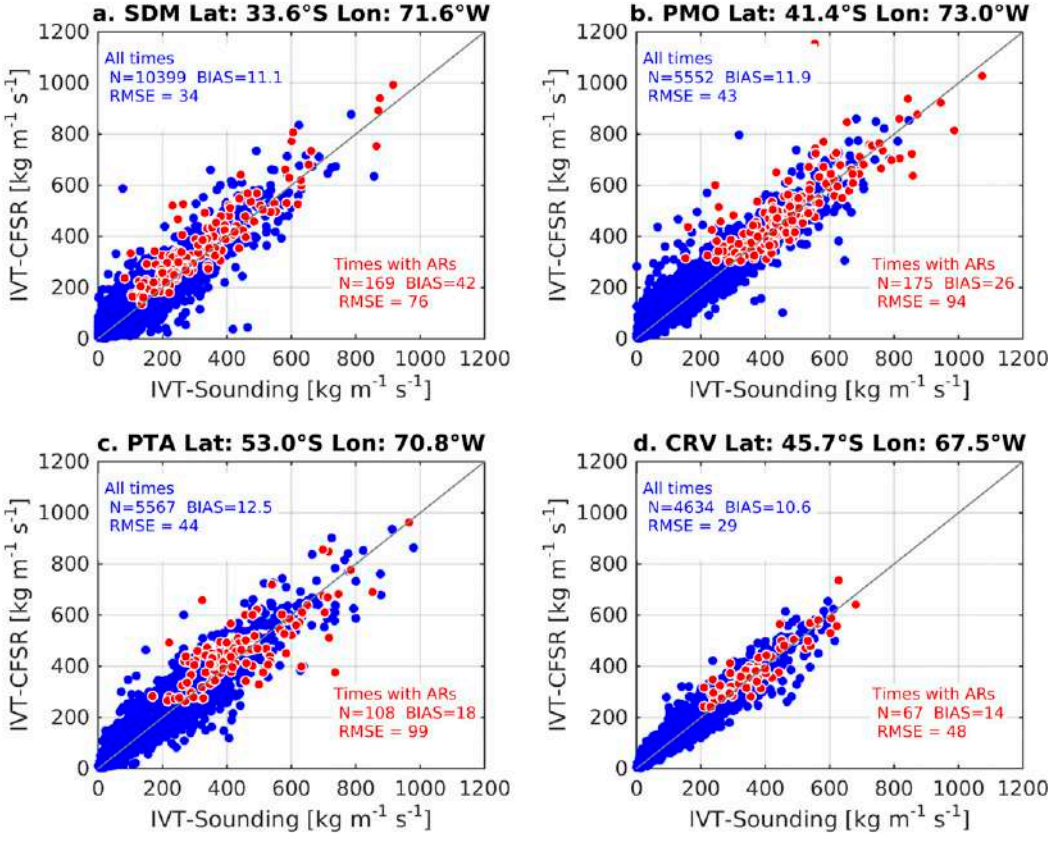

FIG. A1. Scatterplots of IVT sounding vs CFSR IVT ($kg\,m^{-1}\,s^{-1}$) at four sounding sites: (a) Santo Domingo (SDM), (b) Puerto Montt (PMT), (c) Punta Arenas (PTA), and (d) Comodoro Rivadavia (CMR). Blue circles indicate all available times, and red circles indicate only times under AR conditions within the 2001–16 period. Statistics metrics: bias, RMSE, and the straight line derived from the linear regression through the least squares approach between the sounding and CFSR IVT are presented in the top-left corner for all times and in the bottom-right corner for only times under AR conditions.

For all available sounding/CFSR matching times in the 2001–16 period, Fig. A1 highlights a generally reasonable performance of the CFSR data, with a weak overestimation of the water vapor transport especially for values less than ~600 $kg\,m^{-1}\,s^{-1}$. For the subset of times under AR conditions, the bias and RMSE statistics slightly degrade to a greater overestimation and dispersion of the error, although the overestimation is still less than about 10% of the observed IVT. Figure A1 also shows that the overestimation of IVT by CFSR is greater for weaker AR conditions with weaker values of IVT and for ARs occurring on subtropics compared to those in extratropics. This overestimation of IVT at coastal sites by CFSR data during landfalling ARs agrees with the recent comparison of dropsonde-derived IVT with those derived from the GFS analysis product within North Pacific ARs (Ralph et al. 2017b). Although there are differences between the sounding and CFSR IVT datasets here, the overall statistics suggest that the CFSR data are suitable for this study, which uses CFSR reanalyses primarily to detect AR conditions on the west coast of South America and to approximately quantify the IVT strength of ARs.

REFERENCES

Barrett, B. S., D. B. Krieger, and C. P. Barlow, 2011: Multiday circulation and precipitation climatology during winter rain evens of differing intensities in central Chile. *J. Hydrometeor.*, **12**, 1071–1085, https://doi.org/10.1175/2011JHM1377.1.

Blamey, R. C., A. M. Ramos, R. M. Trigo, R. Tomé, and C. J. Reason, 2018: The influence of atmospheric rivers over the South Atlantic on winter rainfall in South Africa. *J. Hydrometeor.*, **19**, 127–142, https://doi.org/10.1175/JHM-D-17-0111.1.

Browning, K. A., 1990: Organization of clouds and precipitation in extratropical cyclones. *Extratropical Cyclones: The Erik Palmén Memorial Volume*, C. W. Newton and E. Holopainen, Eds., Amer. Meteor. Soc., 129–153.

Dettinger, M. D., F. M. Ralph, T. Das, P. J. Neiman, and D. R. Cayan, 2011: Atmospheric rivers, floods and the water resources of California. *Water*, **3**, 445–478, https://doi.org/10.3390/w3020445.

Durre, I., R. S. Vose, and D. B. Wuertz, 2006: Overview of the integrated global radiosonde archive. *J. Climate*, **19**, 53–68, https://doi.org/10.1175/JCLI3594.1.

Eckhardt, S., A. Stohl, H. Wernli, P. James, C. Forster, and N. Spichtinger, 2004: A 15-year climatology of warm conveyor belts. *J. Climate*, **17**, 218–237, https://doi.org/10.1175/1520-0442(2004)017<0218:AYCOWC>2.0.CO;2.

Falvey, M., and R. Garreaud, 2007: Wintertime precipitation episodes in central Chile: Associated meteorological conditions and orographic influences. *J. Hydrometeor.*, **8**, 171–193, https://doi.org/10.1175/JHM562.1.

Garreaud, R., 2009: The Andes climate and weather. *Adv. Geosci.*, **22**, 3–11, https://doi.org/10.5194/adgeo-22-3-2009.

——, 2013: Warm winter storms in central Chile. *J. Hydrometeor.*, **14**, 1515–1534, https://doi.org/10.1175/JHM-D-12-0135.1.

——, and J. Rutllant, 1996: Análisis meteorológico de los aluviones de Antofagasta y Santiago de Chile en el periodo 1991–1993. *Atmósfera*, **9**, 251–271.

Guan, B., and D. E. Waliser, 2015: Detection of atmospheric rivers: Evaluation and application of an algorithm for global studies. *J. Geophys. Res. Atmos.*, **120**, 12 514–12 535, https://doi.org/10.1002/2015JD024257.

——, N. P. Molotch, D. E. Waliser, E. J. Fetzer, and P. J. Neimann, 2010: Extreme snowfall events linked to atmospheric rivers and surface air temperature via satellite measurements. *Geophys. Res. Lett.*, **37**, L20401, https://doi.org/10.1029/2010GL044696.

Hoskins, B. J., and K. I. Hodges, 2005: A new perspective on Southern Hemisphere storm tracks. *J. Climate*, **18**, 4108–4129, https://doi.org/10.1175/JCLI3570.1.

Jenker, J., M. Sprenger, I. Schwenk, C. Schwierz, S. Dierer, and D. Leuenberger, 2010: Detection and climatology of fronts in a high-resolution model reanalysis over the Alps. *Meteor. Appl.*, **17**, 1–18, https://doi.org/10.1002/met.142.

Lamjiri, M. A., M. D. Dettinger, F. M. Ralph, and B. Guan, 2017: Hourly storm characteristics along the U.S. West Coast: Role of atmospheric rivers in extreme precipitation. *Geophys. Res. Lett.*, **44**, 7020–7028, https://doi.org/10.1002/2017GL074193.

Lavers, D., and G. Villarini, 2015: The contributions of atmospheric rivers to precipitation in Europe and the United States. *J. Hydrol.*, **522**, 382–390, https://doi.org/10.1016/j.jhydrol.2014.12.010.

——, ——, R. P. Allan, E. F. Wood, and A. J. Wade, 2012: The detection of atmospheric rivers in atmospheric reanalyses and their links to British winter floods and the large-scale climatic circulation. *J. Geophys. Res.*, **117**, D20106, https://doi.org/10.1029/2012JD018027.

Neiman, P. J., F. M. Ralph, A. B. White, G. A. Wick, J. D. Lundquist, and M. Dettinger, 2008: Meteorological characteristics and overland precipitation impacts of atmospheric river affecting the west coast of Northern America based on eight years of SSM/I satellite observations. *J. Hydrometeor.*, **9**, 22–47, https://doi.org/10.1175/2007JHM855.1.

——, L. J. Schick, F. M. Ralph, M. Hughes, and G. A. Wick, 2011: Flooding in western Washington: The connection to atmospheric rivers. *J. Hydrometeor.*, **12**, 1337–1358, https://doi.org/10.1175/2011JHM1358.1.

Newell, R. E., N. E., Newell, Y. Zhu, and C. Scott, 1992: Tropospheric rivers?—A pilot study. *Geophys. Res. Lett.*, **19**, 2401–2404, https://doi.org/10.1029/92GL02916.

Norte, F. A., A. G. Ulke, S. C. Simonelli, and M. Viale, 2008: The severe zonda wind event of 11 July 2006 east of the Andes Cordillera (Argentine): A case study using the BRAMS model. *Meteor. Atmos. Phys.*, **102**, 1–14, https://doi.org/10.1007/s00703-008-0011-6.

Ralph, F. M., and M. D. Dettinger, 2012: Historical and national perspectives on extreme West Coast precipitation associated with atmospheric rivers during December 2010. *Bull. Amer. Meteor. Soc.*, **93**, 783–790, https://doi.org/10.1175/BAMS-D-11-00188.1.

——, P. J. Neiman, and G. A. Wick, 2004: Satellite and CALJET aircraft observations of atmospheric rivers over the eastern North Pacific Ocean during the winter of 1997/98. *Mon. Wea. Rev.*, **132**, 1721–1745, https://doi.org/10.1175/1520-0493(2004)132<1721:SACAOO>2.0.CO;2.

——, ——, and R. Rotunno, 2005: Dropsonde observations in low-level jets over the northeastern Pacific Ocean from CALJET-1998 and PACJET-2001: Mean vertical profile and

atmospheric river characteristics. *Mon. Wea. Rev.*, **133**, 889–910, https://doi.org/10.1175/MWR2896.1.

——, ——, G. A. Wick, S. I. Gutman, M. D. Dettinger, D. R. Cayan, and A. B. White, 2006: Flooding on California's Russian River: Role of atmospheric rivers. *Geophys. Res. Lett.*, **33**, L13801, https://doi.org/10.1029/2006GL026689.

——, T. Coleman, P. J. Neiman, R. Zamora, and M. D. Dettinger, 2013: Observed impacts of duration and seasonality of atmospheric-river landfalls on soil moisture and runoff in coastal northern California. *J. Hydrometeor.*, **14**, 443–459, https://doi.org/10.1175/JHM-D-12-076.1.

——, and Coauthors, 2017a: Atmospheric rivers emerge as a global science and applications focus. *Bull. Amer. Meteor. Soc.*, **98**, 1969–1973, https://doi.org/10.1175/BAMS-D-16-0262.1.

——, and Coauthors, 2017b: Dropsonde observations of total integrated water vapor transport within North Pacific atmospheric rivers. *J. Hydrometeor.*, **18**, 2577–2596, https://doi.org/10.1175/JHM-D-17-0036.1.

——, M. D. Dettinger, M. M. Cairns, T. Galarneau, and J. Eylander, 2018: Defining "atmospheric river": How the *Glossary of Meteorology* helped resolve a debate. *Bull. Amer. Meteor. Soc.*, **99**, 837–839, https://doi.org/10.1175/BAMS-D-17-0157.1.

Ramos, A. M., R. M. Trigo, M. L. Liberato, and R. Tomé, 2015: Daily precipitation extreme events in the Iberian Peninsula and its association with atmospheric rivers. *J. Hydrometeor.*, **16**, 579–597, https://doi.org/10.1175/JHM-D-14-0103.1.

Rutz, J. J., W. J. Steenburgh, and F. M. Ralph, 2014: Climatological characteristics of atmospheric rivers and their inland penetration over the western United States. *Mon. Wea. Rev.*, **142**, 905–921, https://doi.org/10.1175/MWR-D-13-00168.1.

——, ——, and ——, 2015: The inland penetration of atmospheric rivers over western North America: A Lagrangian analysis. *Mon. Wea. Rev.*, **143**, 1924–1944, https://doi.org/10.1175/MWR-D-14-00288.1.

Saha, S., and Coauthors, 2014: The NCEP Climate Forecast System Reanalysis version 2. *J. Climate*, **27**, 2185–2208, https://doi.org/10.1175/JCLI-D-12-00823.1.

Seluchi, M. E., R. D. Garreaud, F. A. Norte, and A. Saulo, 2006: Influence of the subtropical Andes on baroclinic disturbances: A cold front case study. *Mon. Wea. Rev.*, **134**, 3317–3335, https://doi.org/10.1175/MWR3247.1.

Shields, C. A., and Coauthors, 2018: Atmospheric River Tracking Method Intercomparison Project (ARTMIP): Project goals and experimental design. *Geosci. Model Dev.*, **11**, 2455–2474, https://doi.org/10.5194/gmd-11-2455-2018.

Sodemann, H., and A. Stohl, 2013: Moisture origin and meridional transport in atmospheric rivers and their association with multiple cyclones. *Mon. Wea. Rev.*, **141**, 2850–2868, https://doi.org/10.1175/MWR-D-12-00256.1.

Viale, M., and F. A. Norte, 2009: Strong cross-barrier flow under stable conditions producing intense winter orographic precipitation: A case study over subtropical central Andes. *Wea. Forecasting*, **24**, 1009–1031, https://doi.org/10.1175/2009WAF2222168.1.

——, and M. N. Nuñez, 2011: Climatology of winter orographic precipitation over the subtropical central Andes and associated synoptic and regional characteristics. *J. Hydrometeor.*, **12**, 481–507, https://doi.org/10.1175/2010JHM1284.1.

——, and R. Garreaud, 2015: Orographic effects of the subtropical and extratropical Andes on upwind precipitating clouds. *J. Geophys. Res. Atmos.*, **120**, 4962–4974, https://doi.org/10.1002/2014JD023014.

——, R. Houze Jr., and K. Rasmussen, 2013: Upstream orographic enhancement of a narrow cold-frontal rainband approaching the Andes. *Mon. Wea. Rev.*, **141**, 1708–1730, https://doi.org/10.1175/MWR-D-12-00138.1.

Warner, M. D., C. F. Mass, and E. P. Salathé, 2012: Wintertime extreme precipitation events along the Pacific Northwest coast: Climatology and synoptic evolution. *Mon. Wea. Rev.*, **140**, 2021–2043, https://doi.org/10.1175/MWR-D-11-00197.1.

Wilks, D., 2011: *Statistical Methods in the Atmospheric Sciences.* 3rd ed. International Geophysics Series, Vol. 100, Academic Press, 704 pp.

Zhu, Y., and R. E. Newell, 1994: Atmospheric rivers and bombs. *Geophys. Res. Lett.*, **21**, 1999–2002, https://doi.org/10.1029/94GL01710.

——, and ——, 1998: A proposed algorithm for moisture fluxes from atmospheric rivers. *Mon. Wea. Rev.*, **126**, 725–735, https://doi.org/10.1175/1520-0493(1998)126<0725:APAFMF>2.0.CO;2.